

Article

# Assessment of Low-Reynolds Number $k$ - $\epsilon$ Models in Prediction of a Transitional Flow with Coanda Effect

Xin Nie <sup>1,\*</sup>, Zhihang Chen <sup>1</sup> and Zehui Zhu <sup>2</sup><sup>1</sup> School of Mechanical Engineering, Hangzhou Dianzi University, Hangzhou 310018, China<sup>2</sup> School of Mechanics and Engineering Science, Shanghai University, Shanghai 200444, China

\* Correspondence: nx2000@hdu.edu.cn

**Abstract:** Precise prediction of ventilation flow is essential to create a comfortable, economical, and healthy indoor environment. In the past three decades, the computational fluid dynamics (CFD) method has been used more often, and it is now one of the primary methods for studying building ventilation. The most common CFD method is RANS simulation because of the low cost of computational resources and good accuracy. This paper presents a numerical investigation of a transitional ventilation flow with the Coanda effect, which makes the initial free jet transform into a wall jet. Six low-Reynolds number  $k$ - $\epsilon$  models proposed by Abid (AB), Lam and Bremhorst (LB), Launder and Sharma (LS), Yang and Shih (YS), Abe Kondoh and Nagano (AKN), and Chang, Hsieh and Chen (CHC) are applied. The performance of the six models is evaluated by comparing the computational results with the PIV measurements of Van Hooff et al. The predictions revealed that the LS model has a good approximation of velocity profiles because of its two extra terms in  $k$  and  $\epsilon$  equations, and the AB model is in good agreement with experimental results for predicting the Coanda effect. The LB model provides the worst agreement with experimental data on account of the wrong prediction of turbulent kinetic energy and dissipation rate.

**Keywords:** low-Reynolds number  $k$ - $\epsilon$  model; transitional flow; CFD simulations; Coanda effect; building ventilation



**Citation:** Nie, X.; Chen, Z.; Zhu, Z. Assessment of Low-Reynolds Number  $k$ - $\epsilon$  Models in Prediction of a Transitional Flow with Coanda Effect. *Appl. Sci.* **2023**, *13*, 1783. <https://doi.org/10.3390/app13031783>

Academic Editor: Jawed Mustafa

Received: 4 January 2023

Revised: 25 January 2023

Accepted: 26 January 2023

Published: 30 January 2023



**Copyright:** © 2023 by the authors. Licensee MDPI, Basel, Switzerland. This article is an open access article distributed under the terms and conditions of the Creative Commons Attribution (CC BY) license (<https://creativecommons.org/licenses/by/4.0/>).

## 1. Introduction

Ventilation refers to achieving a comfortable, economical, and healthy environment by regulating indoor air qualities such as air velocity, temperature, and concentration of pollutants in the air. Therefore, accurate prediction of ventilation performance is crucial to improve indoor air quality. Appropriate tools must be in place to predict building ventilation performance. Over the past three decades, there have been many prevalent approaches to predicting ventilation performance, such as analytical models [1–3], empirical models [4,5], experimental measurement models [6–12], and computational fluid dynamics (CFD) models [13–21]. With the development of numerical simulation algorithms and the increase in computing power, the CFD models are more widely used in predicting ventilation performance. The CFD algorithms solve the transport equations of physical quantities of fluid, and many different CFD algorithms are applied in the prediction of ventilation performance, such as RANS (Reynolds-averaged Navier–Stokes) simulations [20,21], LES (large eddy simulations) [22,23], and DNS (direct numerical simulations) [24,25]. However, LES and DNS cost too much in computing resources. Hence, RANS simulations are widely used in the prediction of ventilation performance.

The early experimental and numerical study of ventilation performance was worked by Nielsen [26]. He has constructed a small-scale rectangular model that could change length and height. He has done experiments with about 25 different geometrical shapes at high-Reynolds numbers to investigate the influence of room dimensions on ventilation performance. He illuminated the tracer particles, which are introduced to the air to measure

the streamline pattern, and the velocity profile has been measured by an anemometer. He has reported that a steady two-dimensional flow will arise when the length of the model is less than 3–4 times its height, and if the length of the model gets much longer, a very unsteady flow may take place. He has predicted the ventilation performance by the  $k$ - $\varepsilon$  model. He has further investigated the differences between the experimental and predicted results and found that the prediction results are highly consistent with the experimental data. After Nielsen's research, more and more studies on building ventilation have been proposed. Nevertheless, most of these studies were conducted at fully turbulent Reynolds numbers and did not take into account the Coanda effect, a widespread phenomenon in building ventilation.

Van Hooff et al. [27] have studied the transitional ventilation flow injected from the upper left corner and discharged from the lower right corner in a slot-ventilated enclosure with the inlet Reynolds numbers between 1000 and 2500. They have used two PIV systems to measure velocity and a flow visualization system to observe the jet region and large vortical structures below the jet region. They have reported that the turbulence intensities are higher in the shear layer. Below the shear layer, the turbulence intensities are Re-independent. They have also mentioned that with the increasing of Reynolds numbers, the position of maximum jet velocity in the  $y$  direction increases, the same as the size of the recirculation region in the central area. They have paid close attention to the Coanda effect. The Coanda effect makes the initial free jet (injected not against the ceiling) transform into a wall jet. This phenomenon ensures that the fresh air will not enter the living area too early and can help not make the room's residents feel uncomfortable. The Coanda effect can be caused by the lower pressure generated by the jet entrainment of surrounding fluid between the wall and the free jet.

The experiment done by Van Hooff et al. [27] is numerically investigated by Cao et al. [21]. They have used the low-Reynolds number  $k$ - $\varepsilon$  model of Chang et al. [28] and the SST  $k$ - $\omega$  model [29]. They have studied the influence of inlet boundary conditions on predicting ventilation performance by applying a series of different turbulence intensities and turbulent length scales at  $Re = 1500$ . They have indicated that the simulation results from the two models, as mentioned above, are consistent with the experimental data. They have pointed out that at a transitional Reynolds number, the turbulence intensity of inlet boundary conditions significantly influences the velocity fields. In contrast, the influence of the length scale can be ignored.

However, Cao et al. [21] have ignored the influence of the Coanda effect in the experiment of Van Hooff et al. [27]. Meanwhile, the Coanda effect has enormous implications for the ventilation flow. They have focused too much on the comparison between simulation results and experimental data and lacked the comparison of prediction accuracy between turbulence models. They have only considered the case where the Reynolds number is 1500, resulting in a lack of comparative data at different Reynolds numbers. Therefore, their simulation results cannot be a good comparison with the experimental results of Van Hooff et al. [27].

Over the past years, the low-Reynolds number  $k$ - $\varepsilon$  models have been extensively used to predict turbulent jet flows. However, the ability of the models to predict a transitional ventilation flow with the Coanda effect has received less attention. To address this gap, the mixed ventilation experimentally investigated by Van Hooff et al. [27] is numerically simulated using six low-Reynolds number  $k$ - $\varepsilon$  models. Turbulent models were compared for the prediction of the velocity distribution as well as the influence of the Coanda effect of mixing ventilation in a built environment at low-Reynolds numbers. Due to the Coanda effect and the interaction between the jet region and the recirculation region, the flow is subjected to transition, attachment, separation, and high anisotropy. This paper studies three different Reynolds numbers ( $Re = 1000, 1750, \text{ and } 2500$ , respectively). More details of the six models are given in Section 2.2.

## 2. Geometrical Details and Mathematical Models

### 2.1. Geometrical Details

The reduced-scale experimental configuration of Van Hooff et al. [27] is shown in Figure 1. The test section is a cube with the lengths  $L = 300$  mm. There is a ventilated slot inlet 5 mm below the top of the left wall with a height of 20 mm. The outlet of the test section is at the bottom of the right wall, with a height of 5 mm and a thickness of 8 mm. Downstream of the test section is the overflow section. The overflow section is 120 mm long and 80 mm high. At the top of the right wall of the overflow section, there is a 5 mm high CFD outlet. The working medium is water at 20 °C. The cases studied in this paper are mixing ventilation: the wall jet is injected into the room from the upper left corner, dilutes and mixes with the air in the room, and finally, the mixed air is discharged from the outlet at the lower right corner of the room. This case is one of the most commonly used and researched in the study of building ventilation, which was proposed by Chen [30] and Nielsen [26].

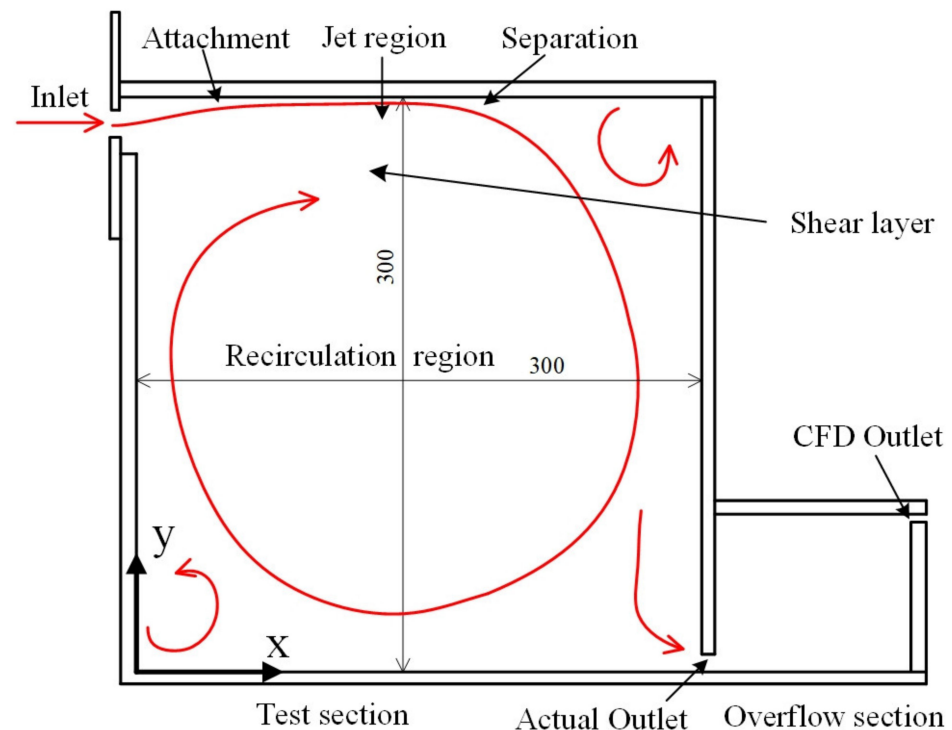


**Figure 1.** The reduced-scale experimental configuration of Van Hooff et al. [27].

### 2.2. Low-Reynolds Number $k-\epsilon$ Model

The low-Reynolds number  $k-\epsilon$  models solve the whole flow field, including the viscous sublayer, instead of the standard  $k-\epsilon$  model, which uses the wall functions to solve the flow in the boundary layer. The significant features of the low-Reynolds number  $k-\epsilon$  models are that the molecular viscosity is introduced into the diffusion term in the  $k$  and  $\epsilon$  equations, and the model constants are multiplied by damping functions to make sure the viscous stresses overwhelm turbulent stresses near the wall (in the viscous sublayer). The low-Reynolds number  $k-\epsilon$  models are more appropriate for complex turbulence with transition flows [31].

In this paper, six low-Reynolds number  $k-\epsilon$  models proposed by Abid (AB) [32], Lam and Bremhorst (LB) [33], Launder and Sharma (LS) [34], Yang and Shih (YS) [35], Abe, Kondoh and Nagano (AKN) [36], and Chang, Hsieh and Chen (CHC) [28] are applied. Six low-Reynolds number  $k-\epsilon$  models used in this paper are briefly introduced as follows:

AB model: this model was proposed to predict the transition process and where the transition starts in the advanced design of modern aerodynamic aircraft. Moreover, it was

validated by predicting a boundary layer transition flow with zero pressure gradient under the influence of free-flow turbulence.

LB model: the special treatment of damping function  $f_\mu$  in the model makes the presence of the wall has a direct or indirect effect on  $f_\mu$ . This model was validated throughout transition processes in fully developed turbulent pipe flow.

LS model: this model fully re-optimized the damping function  $f_\mu$  and  $f_2$ . Two extra source terms were introduced into the  $k$  and  $\varepsilon$  equations to account for the anisotropy in the region near the wall. This model could accurately predict the flow, heat, and mass transfer near a rotating disc.

YS model: this model was designed to capture the gradients in the boundary layer. In this model, the Kolmogorov time scale is introduced in the turbulent time scale, avoiding the possible singularities of the  $\varepsilon$  equation at the walls.

AKN model: this model replaced the friction velocity with the Kolmogorov velocity scale, reproducing the correct turbulent near-wall asymptotic relationship. The AKN model successfully predicts an attached boundary layer flow, separating and re-attaching flow downstream of a backward step.

CHC model: this model could correctly predict near-wall flow restriction behavior while avoiding singular difficulties near the reattachment point. The performance of the CHC model was evaluated by testing fully developed turbulent flows and a recirculating flow in a pipe extension.

More details of the six models will be presented in Section 2.3.

### 2.3. Governing Equations

Continuity equation:

$$\frac{\partial \bar{U}_i}{\partial x_i} = 0 \tag{1}$$

Momentum equation:

$$\bar{U}_j \frac{\partial \bar{U}_i}{\partial x_j} = -\frac{\partial P}{\partial x_i} + \frac{\partial}{\partial x_j} \left[ \nu \left( \frac{\partial \bar{U}_i}{\partial x_j} + \frac{\partial \bar{U}_j}{\partial x_i} \right) - \overline{u_i u_j} \right] \tag{2}$$

with:

$$-\overline{u_i u_j} = \nu_t \left( \frac{\partial \bar{U}_i}{\partial x_j} + \frac{\partial \bar{U}_j}{\partial x_i} \right) - \frac{2}{3} \rho k \delta_{ij} \tag{3}$$

Turbulent eddy viscosity ( $\nu_t$ ):

$$\nu_t = C_\mu f_\mu \frac{k^2}{\tilde{\varepsilon}} \tag{4}$$

Modified dissipation rate ( $\tilde{\varepsilon}$ ):

$$\tilde{\varepsilon} = \varepsilon + D \tag{5}$$

Turbulent kinetic energy ( $k$ ) equation:

$$\bar{U}_j \frac{\partial k}{\partial x_j} = \frac{\partial}{\partial x_j} \left[ \left( \nu + \frac{\nu_t}{\sigma_k} \right) \frac{\partial k}{\partial x_j} \right] + P_k - \tilde{\varepsilon} - D \tag{6}$$

Turbulent energy dissipation rate ( $\tilde{\varepsilon}$ ) equation:

$$\bar{U}_j \frac{\partial \tilde{\varepsilon}}{\partial x_j} = \frac{\partial}{\partial x_j} \left[ \left( \nu + \frac{\nu_t}{\sigma_\varepsilon} \right) \frac{\partial \tilde{\varepsilon}}{\partial x_j} \right] + C_1 f_1 \frac{\tilde{\varepsilon}}{k} P_k - C_2 f_2 \frac{\tilde{\varepsilon}^2}{k} + E \tag{7}$$

Production of turbulent kinetic energy ( $P_k$ ):

$$P_k = \nu_t \left( \frac{\partial \bar{U}_i}{\partial x_j} + \frac{\partial \bar{U}_j}{\partial x_i} \right) \frac{\partial \bar{U}_i}{\partial x_j} \tag{8}$$

The model constants  $C_\mu, C_1, C_2, \sigma_k$ , and  $\sigma_\epsilon$  and extra terms  $D$  and  $E$  of the six low-Reynolds number  $k-\epsilon$  models are defined in Table 1 [28,32–36]. The damping function  $f_\mu, f_1$ , and  $f_2$  are defined in Table 2 [28,32–36].

**Table 1.** Model constants and extra terms in governing equations.

Model	$C_\mu$	$C_1$	$C_2$	$\sigma_k$	$\sigma_\epsilon$	$D$	$E$
AB	0.09	1.45	1.83	1	1.4	0	0
LB	0.09	1.44	1.92	1	1.3	0	0
LS	0.09	1.44	1.92	1	1.3	$2\nu(\partial\sqrt{k}/\partial y)^2$	$2\nu\nu_t(\partial^2\bar{U}/\partial y^2)^2$
YS	0.09	1.44	1.92	1	1.3	0	$\nu\nu_t(\partial^2\bar{U}/\partial y^2)^2$
AKN	0.09	1.44	1.9	1.4	1.4	0	0
CHC	0.09	1.44	1.92	1	1.3	0	0

**Table 2.** Damping function in governing equations.

Model	$f_\mu$	$f_1$	$f_2$
AB	$\tanh(0.008Re_y) \times (1 + 4/Re_t^{0.75})$	1	$1 - 2 \exp(-Re_t^2/36) \times [1 - \exp(-Re_y^2)/12] / 9$
LB	$[1 - \exp(-0.0165Re_y)]^2 \times (1 + 20.5/Re_t)$	$1 + (0.05/f_\mu)^3$	$1 - \exp(-Re_t^2)$
LS	$\exp[-3.4/(1 + Re_t/50)^2]$	1	$1 - 0.3 \exp(-Re_t^2)$
YS	$[1 - \exp(-1.5 \times 10^{-4}Re_y - 5 \times 10^{-7}Re_y^3 - 10^{-10}Re_y^5)]^{0.5}$	1	1
AKN	$\{1 + (5/Re_t^{0.75}) \exp[-(Re_t/200)^2]\} \times [1 - \exp(-y^*/14)]^2$	1	$\{1 - 0.3 \exp[-(Re_t/6.5)^2]\} \times [1 - \exp(-y^*/3.1)]^2$
CHC	$[1 - \exp(-0.0215Re_y)]^2 (1 + 31.66/Re_y^{1.25})$	1	$[1 - 0.01 \exp(-Re_t^2)] \times [1 - \exp(-0.0631Re_y)]$

$Re_y = \sqrt{k}y/\nu$ ;  $Re_t = k^2/(\epsilon\nu)$ ;  $y^* = u_\epsilon y/\nu$ ,  $y$  is the distance from the wall,  $u_\epsilon$  is Kolmogorov velocity scale, and  $u_\epsilon = (\nu\epsilon)^{1/4}$ .

2.4. Solver Settings

In this paper, the simulations are made in Fluent. The second-order upwind scheme is used to discretize the convective term, and the second-order central-difference scheme is used to discretize the diffusive term. The SIMPLEC algorithm is used to handle the velocity–pressure coupling. On account of the difference with the semi-implicit method for pressure-linked equation (SIMPLE) algorithm that the velocity correction equations are settled, the omission terms in SIMPLEC algorithm are less significant than those in SIMPLE. The pseudo-transient approach is used for the under-relaxation of governing equations. The pseudo-transient approach is more suitable for high swirling flows where governing equations may cause numerical stability problems. The globally scaled residual ( $R^\phi$ ) is taken as:

$$R^\phi = \frac{\sum_{cellsP} |\sum_{nb} a_{nb}\phi_{nb} + b - a_p\phi_p|}{\sum_{cellsP} |a_p\phi_p|} \tag{9}$$

where the subscript  $cellsP$  is over all the computational cells  $P$ . The convergence criteria for mass and momentum residuals must be less than  $10^{-6}$ .

### 2.5. Grid Distribution and Grid Independence Study

The grid used for the simulation is shown in Figure 2. The length of the grid in the z-direction is half of the experimental setup because of the use of the symmetry boundary condition. The computational grid is finer near the walls and the region of jet injection and development so that large gradients near the walls and the jet's separation and attachment can be accurately captured. In this paper, the first layer of the grid is placed in the viscous sublayer ( $y^+ < 1$ ) to make sure that the low-Reynolds number  $k$ - $\epsilon$  models can directly solve the variation of physical quantities in the boundary layer.

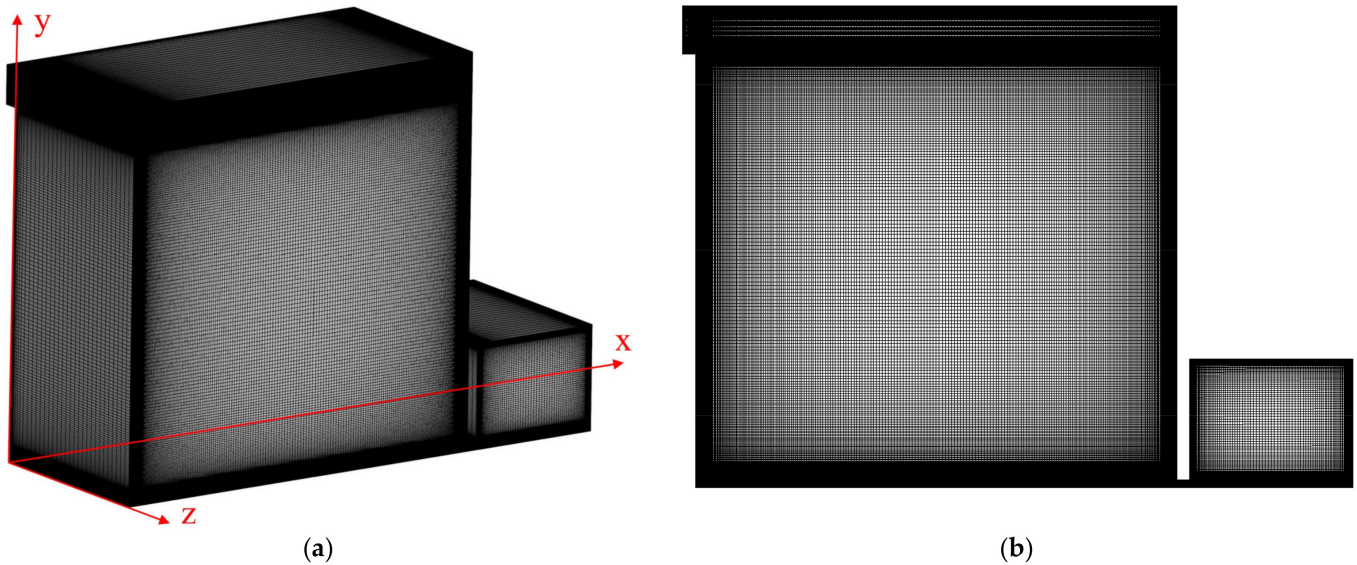


**Figure 2.** (a) Computational grid distribution; (b) grid in xy plane.

To verify that the grid is independent of the final calculated flow results, three grid sizes  $251 \times 315 = 79,065$ ,  $301 \times 365 = 109,865$ , and  $351 \times 415 = 145,665$  of the test section are used for grid independence verification. As shown in Figure 3, with the increase in grid numbers, the dimensionless x-velocity profiles calculated by the AB model at  $x/L = 0.07$  of the three grid sizes have a good consistency. Note  $U_M$  is the local maximum time-averaged x-velocity. This shows that the increase in grid density has little impact on the results. Considering the available computing resources and numerical simulation cycles, a grid size of  $301 \times 365 = 109,865$  is chosen for simulation. The minimum orthogonal quality of the grid is 0.99, the maximum skewness is 0.004, and the maximum aspect ratio is 19.14.

### 2.6. Boundary Conditions

The boundary conditions selected in this paper are as close as possible to the experiments. The Reynolds numbers at the jet inlet are 1000, 1750, and 2500, respectively [27]. Therefore, the boundary condition of jet inlet is set to velocity inlet and the velocity is 0.05 m/s, 0.0875 m/s, and 0.125 m/s corresponding to three different Reynolds numbers. The turbulent intensity  $I = 0.01$ , which is due to a low level of turbulence at the inlet and the turbulent length scale, is taken as the height of the jet inlet ( $L = 0.02$  m). The turbulent kinetic energy and dissipation rate at the jet inlet are calculated from the following assumed forms:  $k = 2/3(\overline{U_i I})^2$  and  $\epsilon = C_\mu^{0.75} k^{1.5} / (0.07L)$ . The no-slip boundary conditions ( $\overline{U_i} = 0$ ) are imposed along the solid walls. The boundary conditions for turbulent kinetic energy and dissipation rate at the solid walls are summarized in Table 3 [28,32–36]. The CFD outlet is set to the pressure outlet boundary condition with a static pressure of 0 Pascals.

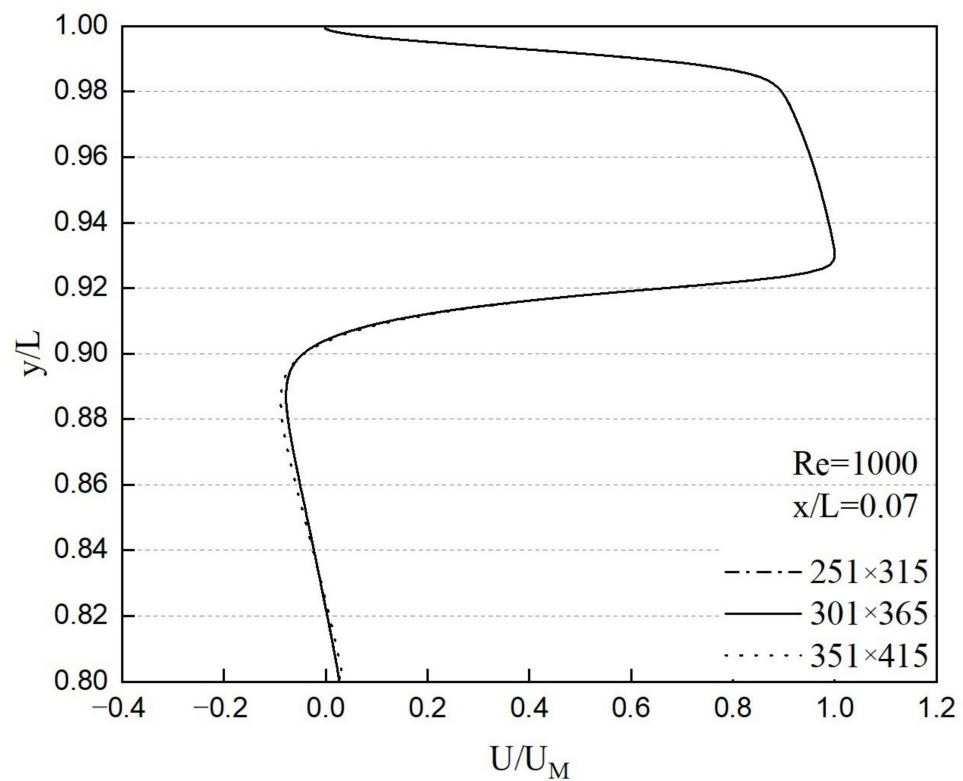


Figure 3. Grid independence test predicted by AB model.

Table 3. Turbulent kinetic energy and dissipation rate boundary conditions of six low-Reynolds number  $k-\epsilon$  models.

Model	$k_{bc}$	$\epsilon_{bc}$
AB	$k_w = 0$	$\epsilon_w = \nu(\partial^2 k / \partial y^2)$
LB	$k_w = 0$	$\epsilon_w = \nu(\partial^2 k / \partial y^2)$
LS	$(\partial k / \partial y)_w = 0$	$\epsilon_w = 0$
YS	$k_w = 0$	$\epsilon_w = 2\nu(\partial\sqrt{k} / \partial y)^2$
AKN	$k_w = 0$	$\epsilon_w = 2\nu(k_p / y_p^2)$
CHC	$k_w = 0$	$\epsilon_w = \nu(\partial^2 k / \partial y^2)$

Subscript  $P$  is the first node away from the wall.

### 3. Results and Discussion

The evaluation of six low-Reynolds number  $k-\epsilon$  models, namely the AB, LB, LS, YS, AKN, and CHC models, have been applied in this paper to investigate their effects on building ventilation parameters such as velocity distributions, Coanda effect, etc. The flow quantities predicted by the models are compared with the experiment data of Van Hooff et al. [27].

#### 3.1. Mean Velocity Profiles

Figure 4 compares the dimensionless  $x$ -velocity ( $U/U_M$ ) profiles predicted by six low-Reynolds  $k-\epsilon$  number models with PIV measurements at  $x/L = 0.07, 0.27$  and  $0.47$  for  $Re = 1000, 1750,$  and  $2500,$  respectively.

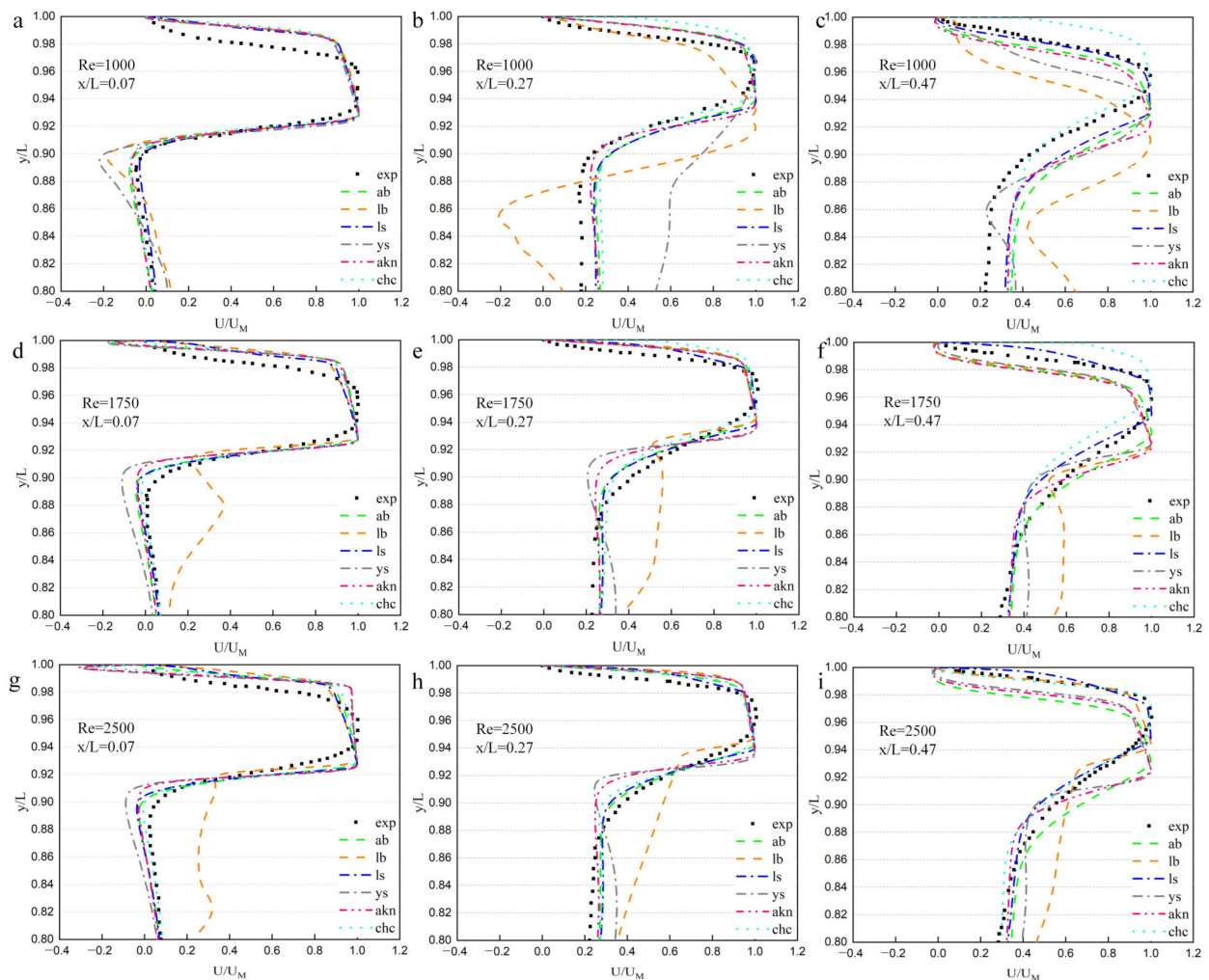


**Figure 4.** Comparison of mean dimensionless x-velocity profiles measured by PIV and modeled by six low-Reynolds number  $k-\varepsilon$  models. (a)  $Re = 1000$ ,  $x/L = 0.07$ ; (b)  $Re = 1000$ ,  $x/L = 0.27$ ; (c)  $Re = 1000$ ,  $x/L = 0.47$ ; (d)  $Re = 1750$ ,  $x/L = 0.07$ ; (e)  $Re = 1750$ ,  $x/L = 0.27$ ; (f)  $Re = 1750$ ,  $x/L = 0.47$ ; (g)  $Re = 2500$ ,  $x/L = 0.07$ ; (h)  $Re = 2500$ ,  $x/L = 0.27$ ; (i)  $Re = 2500$ ,  $x/L = 0.47$ .

At  $x/L = 0.07$  (Figure 4a,d,g), the YS model predicts erroneous results, especially under the jet region ( $y/L < 0.94$ ), and the LB model underpredicts the velocity value. The other four turbulence models predict better results, but there are still some problems: the thickness of the wall jet is too thick. In Figure 4d,g, the YS, AKN, and CHC models predict negative dimensionless velocities near the wall, which means that the jets predicted by these three models are attached to the wall too late.

At  $x/L = 0.27$  (Figure 4b,e,h), the LB and YS models still predict totally wrong results of velocity profiles. The AKN model provides a good agreement with the measurement data at  $Re = 1000$  while performing poor at  $Re = 1750$  and  $2500$ . At  $x/L = 0.07$  and  $0.27$ , the thickness of boundary layer predicted by six models is thinner than that of PIV measurements, where the jet has not yet separated from the wall. This may be due to a seriously too-low level of  $\varepsilon$  near the wall in separated flows or flows approaching separation [37]. When the flow does not separate from the wall (at  $x/L = 0.07$  and  $0.27$ ), the results obtained by AB and LS models are more accurate.

At  $x/L = 0.47$  (Figure 4c,f,i), all six models predict negative dimensionless velocities near the wall, indicating that the boundary layer predicted by the six models starts to separate from the wall. These models underpredict the position of separation of the wall

jet. In this situation, only the LS model shows the best agreement of the boundary layer with the PIV measurements.

Most of the low-Reynolds number  $k-\epsilon$  models (except the LB and YS models) predict almost the same velocity profiles in the recirculation region ( $y/L < 0.9$ ) but cannot predict well in the boundary layer ( $0.97 < y/L$ ) and shear layer ( $0.9 < y/L < 0.94$ ) between the jet region and recirculation region. There is a large velocity gradient in the boundary layer and shear layer, which leads to a strong anisotropic effect. The isotropic Boussinesq hypothesis has some errors in those regions.

The LB model provides the worst agreement with experiment data. The velocity predicted by the LB model is always too large in the recirculation region. In general, the LS model performs best in predicting velocity profiles. Because the extra  $D$  and  $E$  terms of the  $k$  and  $\epsilon$  equations in the LS model are expressed as  $2\nu\left(\partial\sqrt{k}/\partial y\right)^2$  and  $2\nu\nu_t\left(\partial^2\bar{U}/\partial y^2\right)^2$ , respectively, rather than most of the turbulence models used in this paper, the extra terms  $D$  and  $E$  are equal to 1. The  $D$  term in the LS model is added to consider that the dissipation of kinetic energy is not isotropic in the viscous sublayer, and the  $E$  term is aimed to make the simulation result of kinetic energy fits better with some experiments. The two extra terms can cover the shortage of isotropic Boussinesq hypothesis in some ways [38].

Table 4 shows the relative error of mean velocity. It is calculated according to the experimental data of Van Hooff et al. [27]. It can be seen that the relative error values predicted by all six models at  $x/L = 0.07$  are higher than those at  $x/L = 0.27$  and  $0.47$ . The minimum average relative error is 22.65% predicted by the LS model, while the maximum average relative error is 132.80% predicted by the LB model. This result is the same as the previously mentioned conclusion.

**Table 4.** Relative error of mean velocity predicted by six low-Reynolds number  $k-\epsilon$  models.

Model	AB	LB	LS	YS	AKN	CHC
Relative Error						
Re = 1000 $x/L = 0.07$	72.33%	120.68%	37.58%	56.61%	18.76%	32.29%
Re = 1000 $x/L = 0.27$	23.65%	79.48%	22.65%	101.04%	17.86%	20.57%
Re = 1000 $x/L = 0.47$	34.59%	84.89%	23.12%	37.10%	34.42%	20.48%
Re = 1750 $x/L = 0.07$	95.07%	586.95%	50.44%	204.50%	89.86%	41.21%
Re = 1750 $x/L = 0.27$	9.39%	38.21%	10.18%	25.19%	17.30%	21.56%
Re = 1750 $x/L = 0.47$	11.42%	30.89%	7.62%	17.61%	13.87%	21.99%
Re = 2500 $x/L = 0.07$	39.40%	193.89%	35.07%	83.45%	50.95%	26.96%
Re = 2500 $x/L = 0.27$	8.16%	36.90%	10.31%	25.50%	15.57%	21.43%
Re = 2500 $x/L = 0.47$	16.68%	23.30%	6.86%	17.25%	13.37%	16.02%
Average relative error	34.52%	132.80%	22.65%	63.14%	30.22%	24.72%

### 3.2. Coanda Effect

Figure 5 shows the position of the maximum dimensionless  $x$ -velocities of the jet. This can be used to depict how the jet develops in the test section. It can be clearly observed that the jet moves upward first and then downward. The initial free jet develops into a wall

jet because of the Coanda effect. It can be attributed to the lower pressure generated by jet entrainment of surrounding fluid between the wall and the free jet.

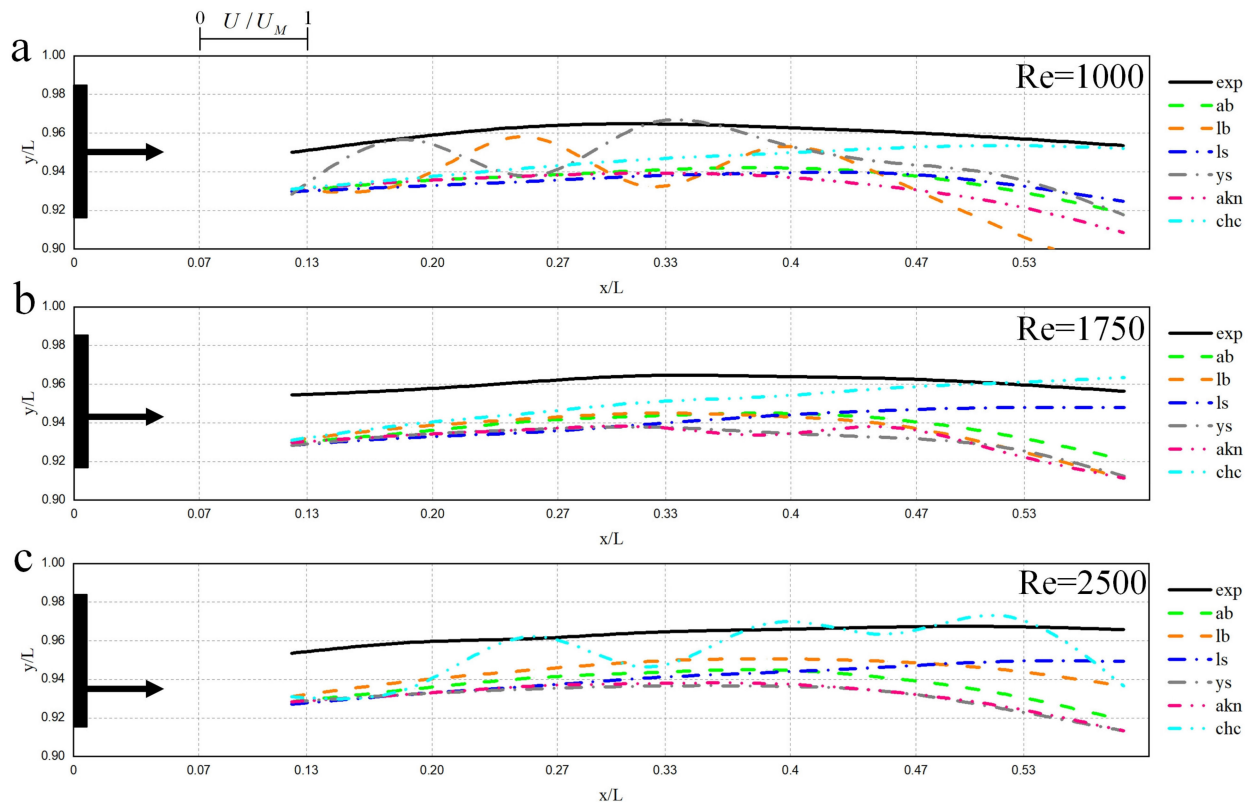


**Figure 5.** Comparison of the position of the maximum dimensionless  $x$ -velocities of the jet measured by PIV and modeled by six low-Reynolds number  $k$ - $\epsilon$  models. (a)  $Re = 1000$ ; (b)  $Re = 1750$ ; (c)  $Re = 2500$ .

The maximum dimensionless  $x$ -velocities predicted by all six models are located below the experimental data. At  $Re = 1000$ , the maximum value of  $y/L$  appears at  $0.27 < x/L < 0.33$ . At  $Re = 1750$ , the maximum value of  $y/L$  appears at  $0.33 < x/L < 0.4$ , and at  $Re = 2500$ , the maximum value of  $y/L$  appears at  $0.4 < x/L < 0.47$ . Behind these positions, it begins to decrease. This phenomenon indicates that the attached wall jet is separating from the wall. Moreover, with the increase in  $Re$ , the separation of the wall jet occurs later.

In Figure 5a, it can be seen that the LB and YS models perform quite poorly for  $Re = 1000$ . The maximum value of  $y/L$  predicted by the CHC model is still increasing after  $x/L = 0.53$ . The trend of the results predicted by the AB and AKN models is in good agreement with the experimental results. In Figure 5b,c, the LB and YS models predict better results for  $Re = 1750$  and  $Re = 2500$  than the result for  $Re = 1000$ . By contrast, the CHC model predicts the worst result when  $Re$  is high ( $Re = 2500$ ).

The LS model always overpredicts the position of separation of the wall jet, and the AB model has the best result in predicting the Coanda effect.

### 3.3. Turbulent Kinetic Energy and Dissipation Rate Profiles

As essential turbulent physical quantities describing the flow state, it is necessary to discuss further the capabilities of the six low-Reynolds number  $k$ - $\epsilon$  models for predicting turbulent kinetic energy and dissipation rate of the transitional ventilation flow with the Coanda effect. Figures 6 and 7 illustrate the profiles of turbulent kinetic energy and dissipation rate. It is shown that most of the models predict two peak values of turbulent kinetic energy and dissipation rate in the boundary layer and shear layer ( $0.9 < y/L < 0.94$ ) because

of the great velocity gradients in these two regions. The LS model predicts tremendous values of turbulent kinetic energy and dissipation rate near the wall. The best experimental setup reveals that the turbulent dissipation rate rises to an unknown constant value approaching the wall [38]. The turbulent kinetic energy is equal to 0 because of the no-slip condition. Thus, the boundary conditions of the LS model's turbulent kinetic energy and dissipation rate ( $(\partial k / \partial y)_w = 0$  and  $\varepsilon_w = 0$ ) may be inappropriate (see details in Table 2). The LB model predicts a too-low level of turbulent kinetic energy (close to 0) and a too-high level of turbulent dissipation rate in the recirculation region ( $y/L < 0.9$ ), which leads to the inaccurate prediction of velocity, as mentioned in Section 3.1. At  $x/L = 0.07$ , the AKN model cannot capture the second peak of turbulent kinetic energy. Moreover, at  $Re = 2500$ , the YS model cannot capture that, either. The turbulent kinetic energy and dissipation rate predicted by the CHC model seems more realistic than other models because this model can actually capture the two peaks of  $k$  and  $\varepsilon$  without unreasonably large values.

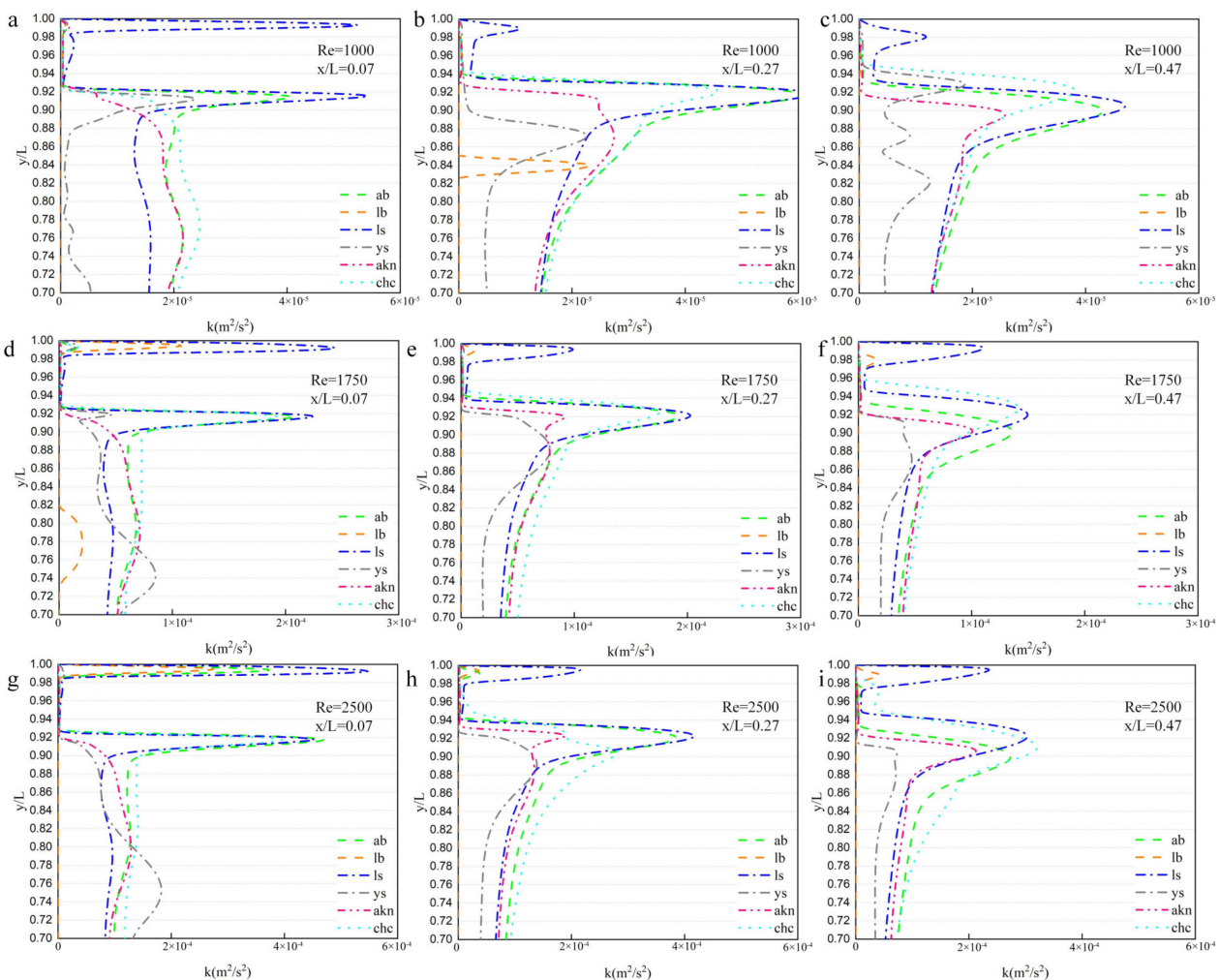


**Figure 6.** Comparison of turbulent kinetic energy profiles measured by PIV and modeled by six low-Reynolds number  $k$ - $\varepsilon$  models. (a)  $Re = 1000$ ,  $x/L = 0.07$ ; (b)  $Re = 1000$ ,  $x/L = 0.27$ ; (c)  $Re = 1000$ ,  $x/L = 0.47$ ; (d)  $Re = 1750$ ,  $x/L = 0.07$ ; (e)  $Re = 1750$ ,  $x/L = 0.27$ ; (f)  $Re = 1750$ ,  $x/L = 0.47$ ; (g)  $Re = 2500$ ,  $x/L = 0.07$ ; (h)  $Re = 2500$ ,  $x/L = 0.27$ ; (i)  $Re = 2500$ ,  $x/L = 0.47$ .

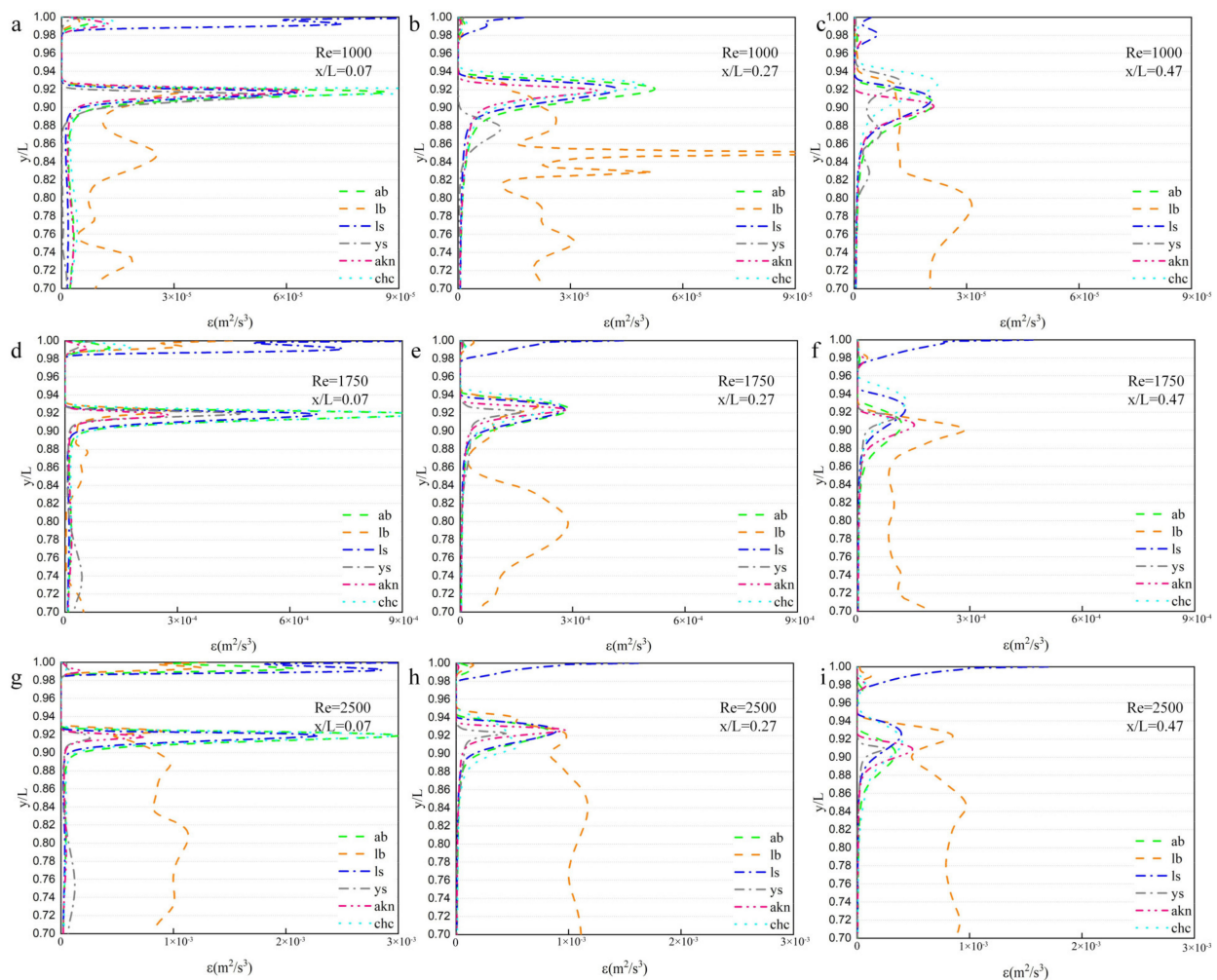


**Figure 7.** Comparison of dissipation rate of turbulent kinetic energy profiles measured by PIV and modeled by six low-Reynolds number  $k-\epsilon$  models. (a)  $Re = 1000$ ,  $x/L = 0.07$ ; (b)  $Re = 1000$ ,  $x/L = 0.27$ ; (c)  $Re = 1000$ ,  $x/L = 0.47$ ; (d)  $Re = 1750$ ,  $x/L = 0.07$ ; (e)  $Re = 1750$ ,  $x/L = 0.27$ ; (f)  $Re = 1750$ ,  $x/L = 0.47$ ; (g)  $Re = 2500$ ,  $x/L = 0.07$ ; (h)  $Re = 2500$ ,  $x/L = 0.27$ ; (i)  $Re = 2500$ ,  $x/L = 0.47$ .

#### 4. Conclusions

This study presents simulations of transitional ventilation flow in building environments with the Coanda effect predicted by six low-Reynolds number  $k-\epsilon$  models for three different Reynolds numbers ( $Re = 1000$ ,  $1750$ , and  $2500$ ).

The geometrical details and boundary conditions used in the simulation are as similar as possible to those in the experiment of Van Hooff et al. [27]. The flow is subjected to transition, attachment, separation, and high anisotropy because of the Coanda effect, the interaction of the jet region with the recirculation region, etc. Some of these specific conclusions are summarized below:

- All six models predict a thinner boundary layer than that in experiments because of a seriously too-low level of  $\epsilon$  near the wall in separated flows or flows approaching separation;
- The AB, LB, YS, AKN, and CHC models underpredict the position of separation of the wall jet, while the LS model overpredicts the position of separation of the wall jet;
- The LB and YS models cannot predict the Coanda effect well when the Reynolds number is low ( $Re = 1000$ ), but when the Reynolds number increases to  $1750$  and  $2500$ , the LB and YS models perform better—the CHC model is the exact opposite;
- The LB model predicts unreasonable results of turbulent kinetic energy and dissipation rate, leading to the wrong velocity profile predictions;

- The LS model has a good approximation of velocity profiles, and the AB model is very suitable for predicting the Coanda effect.

**Author Contributions:** Software, X.N.; Validation, Z.C.; Data curation, Z.Z.; Writing—original draft, Z.C.; Writing—review & editing, Z.Z.; Funding acquisition, X.N. All authors have read and agreed to the published version of the manuscript.

**Funding:** This research was funded by [Zhejiang Province Bellwethers Projects] grant number [2023C03126]. The APC was funded by [Zhejiang Province Bellwethers Projects].

**Institutional Review Board Statement:** Not applicable.

**Informed Consent Statement:** Not applicable.

**Data Availability Statement:** All data included in this study are available upon request by contact with the corresponding author.

**Conflicts of Interest:** The authors declare no conflict of interest.

## References

1. Linden, P.F. The fluid mechanics of natural ventilation. *Annu. Rev. Fluid Mech.* **1999**, *31*, 201–238. [\[CrossRef\]](#)
2. Coffey, C.J.; Hunt, G.R. Ventilation effectiveness measures based on heat removal: Part 2. Application to natural ventilation flows. *Build. Environ.* **2007**, *42*, 2249–2262. [\[CrossRef\]](#)
3. Ji, Y.; Cook, M.J.; Hanby, V. CFD modelling of natural displacement ventilation in an enclosure connected to an atrium. *Build. Environ.* **2007**, *42*, 1158–1172. [\[CrossRef\]](#)
4. Allocca, C.; Chen, Q.; Glicksman, L.R. Design analysis of single-sided natural ventilation. *Energy Build.* **2003**, *35*, 785–795. [\[CrossRef\]](#)
5. Larsen, T.S.; Heiselberg, P. Single-sided natural ventilation driven by wind pressure and temperature difference. *Energy Build.* **2008**, *40*, 1031–1040. [\[CrossRef\]](#)
6. Norton, T.; Grant, J.; Fallon, R.; Sun, D.-W. Assessing the ventilation effectiveness of naturally ventilated livestock buildings under wind dominated conditions using computational fluid dynamics. *Biosyst. Eng.* **2009**, *103*, 78–99. [\[CrossRef\]](#)
7. Wang, M.; Chen, Q. Assessment of Various Turbulence Models for Transitional Flows in an Enclosed Environment (RP-1271). *HVACR Res.* **2009**, *15*, 1099–1119. [\[CrossRef\]](#)
8. Karava, P.; Stathopoulos, T.; Athienitis, A.K. Airflow assessment in cross-ventilated buildings with operable façade elements. *Build. Environ.* **2011**, *46*, 266–279. [\[CrossRef\]](#)
9. Magnier, L.; Zmeureanu, R.; Derome, D. Experimental assessment of the velocity and temperature distribution in an indoor displacement ventilation jet. *Build. Environ.* **2012**, *47*, 150–160. [\[CrossRef\]](#)
10. Yang, T.; Wright, N.G.; Etheridge, D.W.; Quinn, A.D. A Comparison of CFD and Full-scale Measurements for Analysis of Natural Ventilation. *Int. J. Vent.* **2016**, *4*, 337–348. [\[CrossRef\]](#)
11. Li, Y.; Zhou, J.; Long, E.; Meng, X. Experimental study on thermal performance improvement of building envelopes by integrating with phase change material in an intermittently heated room. *Sustain. Cities Soc.* **2018**, *38*, 607–615. [\[CrossRef\]](#)
12. Wang, J.; Meng, Q.; Tan, K.; Zhang, L.; Zhang, Y. Experimental investigation on the influence of evaporative cooling of permeable pavements on outdoor thermal environment. *Build. Environ.* **2018**, *140*, 184–193. [\[CrossRef\]](#)
13. Sun, S.; Xu, X.; Lao, Z.; Liu, W.; Li, Z.; Higuera García, E.; He, L.; Zhu, J. Evaluating the impact of urban green space and landscape design parameters on thermal comfort in hot summer by numerical simulation. *Build. Environ.* **2017**, *123*, 277–288. [\[CrossRef\]](#)
14. Moujalled, B.; Ouméziane, Y.A.; Moissette, S.; Bart, M.; Lanos, C.; Samri, D. Experimental and numerical evaluation of the hygrothermal performance of a hemp lime concrete building: A long term case study. *Build. Environ.* **2018**, *136*, 11–27. [\[CrossRef\]](#)
15. Fan, J.; Dong, H.; Xu, X.; Teng, D.; Yan, B.; Zhao, Y. Numerical Investigation on the Influence of Mechanical Draft Wet-Cooling Towers on the Cooling Performance of Air-Cooled Condenser with Complex Building Environment. *Energies* **2019**, *12*, 4560. [\[CrossRef\]](#)
16. Johra, H.; Heiselberg, P.; Dréau, J.L. Influence of envelope, structural thermal mass and indoor content on the building heating energy flexibility. *Energy Build.* **2019**, *183*, 325–339. [\[CrossRef\]](#)
17. Ganesh, G.A.; Sinha, S.L.; Verma, T.N. Numerical simulation for optimization of the indoor environment of an occupied office building using double-panel and ventilation radiator. *J. Build. Eng.* **2020**, *29*, 101139. [\[CrossRef\]](#)
18. Raj, B.P.; Meena, C.S.; Agarwal, N.; Saini, L.; Khahro, S.H.; Subramaniam, U.; Ghosh, A. A Review on Numerical Approach to Achieve Building Energy Efficiency for Energy, Economy and Environment (3E) Benefit. *Energies* **2021**, *14*, 4487. [\[CrossRef\]](#)
19. Sun, Y.; Wilson, R.; Liu, H.; Wu, Y. Numerical investigation of a smart window system with thermotropic Parallel Slat Transparent Insulation Material for building energy conservation and daylight autonomy. *Build. Environ.* **2021**, *203*, 108048. [\[CrossRef\]](#)
20. Moureh, J.; Flick, D. Wall air-jet characteristics and airflow patterns within a slot ventilated enclosure. *Int. J. Therm. Sci.* **2003**, *42*, 703–711. [\[CrossRef\]](#)

21. Cao, S.-J.; Meyers, J. Influence of turbulent boundary conditions on RANS simulations of pollutant dispersion in mechanically ventilated enclosures with transitional slot Reynolds number. *Build. Environ.* **2013**, *59*, 397–407. [[CrossRef](#)]
22. Zhang, W.; Chen, Q. Large eddy simulation of indoor airflow with a filtered dynamic subgrid scale model. *Int. J. Heat Mass Transf.* **2000**, *43*, 3219–3231. [[CrossRef](#)]
23. Wang, M.; Chen, Q. On a Hybrid RANS/LES Approach for Indoor Airflow Modeling (RP-1271). *HVACR Res.* **2010**, *16*, 731–747. [[CrossRef](#)]
24. Shishkina, O.; Shishkin, A.; Wagner, C. Simulation of turbulent thermal convection in complicated domains. *J. Comput. Appl. Math.* **2009**, *226*, 336–344. [[CrossRef](#)]
25. Wagner, C.; Shishkin, A.; Shishkina, O. *The Use of Direct Numerical Simulations for Solving Industrial Flow Problems*; Springer: Dordrecht, The Netherlands, 2011; Volume 15, pp. 397–404.
26. Nielsen, P.V. *Flow in Air Conditioned Rooms: Model Experiments and Numerical Solution of the Flow Equations*; Technical University of Denmark: Copenhagen, Denmark, 1974.
27. Van Hooff, T.; Blocken, B.; Defraeye, T.; Carmeliet, J.; van Heijst, G.J.F. PIV measurements and analysis of transitional flow in a reduced-scale model: Ventilation by a free plane jet with Coanda effect. *Build. Environ.* **2012**, *56*, 301–313. [[CrossRef](#)]
28. Chang, K.C.; Hsieh, W.D.; Chen, C.S. A Modified Low-ReynoldsNumber Turbulence Model Applicable to Recirculating Flow in Pipe Expansion. *J. Fluids Eng.* **1995**, *117*, 417–423. [[CrossRef](#)]
29. Menter, F.R. Two-equation eddy-viscosity turbulence models for engineering applications. *AIAA J.* **1994**, *32*, 1598–1605. [[CrossRef](#)]
30. Chen, Q. Comparison of Different  $k-\epsilon$  Models for Indoor Air Flow Computations. *Numer. Heat Transf. Part B Fundam.* **1995**, *28*, 353–369. [[CrossRef](#)]
31. Rathore, S.K.; Das, M.K. Numerical investigation on the performance of low-Reynolds number  $k-\epsilon$  model for a buoyancy-opposed wall jet flow. *Int. J. Heat Mass Transf.* **2016**, *95*, 636–649. [[CrossRef](#)]
32. Abid, R. Evaluation of two-equation turbulence models for predicting transitional flows. *Int. J. Eng. Sci.* **1993**, *31*, 831–840. [[CrossRef](#)]
33. Lam, C.K.G.; Bremhorst, K. A Modified Form of the  $k-\epsilon$  Model for Predicting Wall Turbulence. *J. Fluids Eng.* **1981**, *103*, 456–460. [[CrossRef](#)]
34. Launder, B.E.; Sharma, B.I. Application of the energy-dissipation model of turbulence to the calculation of flow near a spinning disc. *Lett. Heat Mass Transf.* **1974**, *1*, 131–138. [[CrossRef](#)]
35. Yang, Z.; Shih, T.H. New time scale based  $k-\epsilon$  model for near-wall turbulence. *AIAA J.* **1993**, *31*, 1191–1198. [[CrossRef](#)]
36. Abe, K.; Kondoh, T.; Nagano, Y. A new turbulence model for predicting fluid flow and heat transfer in separating and reattaching flows-I. Flow field calculations. *Int. J. Heat Mass Transf.* **1994**, *37*, 139–151. [[CrossRef](#)]
37. Hosseinalipour, S.M.; Mujumdar, A.S. Comparative Evaluation of Different Turbulence Models for Confined Impinging and Opposing Jet Flows. *Numer. Heat Transf. Part A Appl.* **1995**, *28*, 647–666. [[CrossRef](#)]
38. Versteeg, H.K.; Malalasekera, W. *An Introduction to Computational Fluid Dynamics: The Finite Volume Method*, 2nd ed.; Person Education Limited: London, UK, 2007; pp. 75–80.

**Disclaimer/Publisher’s Note:** The statements, opinions and data contained in all publications are solely those of the individual author(s) and contributor(s) and not of MDPI and/or the editor(s). MDPI and/or the editor(s) disclaim responsibility for any injury to people or property resulting from any ideas, methods, instructions or products referred to in the content.